Vector Finite Difference Modesolver for Anisotropic Dielectric Waveguides

Arman B. Fallahkhair, *Student Member, IEEE*, Kai S. Li, and
Thomas E. Murphy, *Senior Member, IEEE, Member, OSA*

***Abstract*—We describe a new full-vector finite difference discretization, based upon the transverse magnetic field components, for calculating the electromagnetic modes of optical waveguides with transverse, nondiagonal anisotropy. Unlike earlier finite difference approaches, our method allows for the material axes to be arbitrarily oriented, as long as one of the principal axes coincides with the direction of propagation. We demonstrate the capabilities of the method by computing the circularly-polarized modes of a magnetooptical waveguide and the modes of an off-axis poled anisotropic polymer waveguide.**

***Index Terms*—Anisotropic media, birefringence, dielectric waveguides, Faraday effect, finite difference methods, optical propagation in anisotropic media.**

I. INTRODUCTION

AN OPTICAL waveguide modesolver is one of the most important tools used in designing integrated optical circuits. Several techniques are commonly used to compute the electromagnetic modes of waveguides, including finite element methods, mode-matching techniques, method of lines, and finite difference methods [1]. Many methods completely neglect the anisotropy of the constituent materials. Of those that do account for material anisotropy, most require that the permittivity tensor be diagonal when expressed in the coordinate system of the waveguide. Others allow for nondiagonal tensors, but require that the off-diagonal elements be small in comparison to the diagonal terms [2]–[4], or that the waveguide be weakly-guiding [5]. Although these techniques are adequate for many optical waveguides, they cannot be easily applied to waveguides in which the anisotropy is oriented along an oblique axis, or magnetooptic materials for which the eigenstates are circularly polarized.

A few finite element approaches have been developed to accurately model waveguides comprised of nondiagonal anisotropic materials [6]–[13]. Most of these use the transverse magnetic field formulation, which eliminates spurious modes and simplifies the boundary conditions at interfaces.

The transverse magnetic field formulation is also widely used in finite difference methods [14]–[17], some of which have been extended to include anisotropic materials with diagonal permittivities [18], [19].

Any finite element discretization, when applied to a rectangular mesh could yield equations similar to those obtained by finite difference analysis. Nonetheless, finite difference methods have broad appeal because they offer an explicit, closed-form expression for the differential operator, and the solutions obtained by finite difference methods can be easily visualized, manipulated, or post-processed without the need for mesh interpolation. Despite the simplicity and appeal of the finite difference methods, there have been comparatively few reports of finite difference modesolvers or beam propagation methods that can accommodate anisotropic materials for which the permittivity tensor is nondiagonal [20].

We describe here a full-vector finite-difference discretization that allows for more general, nondiagonal, and possibly spatially-varying anisotropy. The only constraint of the method is that one of the material principal axes must coincide with the direction of propagation, that is, the waveguide (and material anisotropy) must be symmetric under the reflection $z \rightarrow -z$. The method computes the transverse magnetic field components H_x and H_y, while enforcing the zero-divergence condition of $\mathbf{H}$ to ensure against spurious modes. We present examples including a magnetooptical waveguide with circularly-polarized modes and a tilted-axis poled polymer waveguide.

II. ANISOTROPIC EIGENMODE EQUATIONS

We consider here transverse anisotropic materials, constrained so that one of the material principal axes points in the direction of the waveguide. Under this assumption, the permittivity tensor takes the form

$$\boldsymbol{\epsilon} \equiv \epsilon_0 \begin{bmatrix} \epsilon_{xx} & \epsilon_{xy} & 0 \\ \epsilon_{yx} & \epsilon_{yy} & 0 \\ 0 & 0 & \epsilon_{zz} \end{bmatrix}. \tag{1}$$

While it is generally possible to find a rotated coordinate system in which this permittivity tensor is diagonal, it is often inconvenient to apply finite difference methods in such a rotated reference frame because the waveguide boundaries would be oriented at oblique angles to the finite difference grid. Furthermore, in waveguides containing two or more anisotropic regions with different orientations, it would be impossible to diagonalize $\boldsymbol{\epsilon}$ for all materials under the same rotation. Lastly, in a magnetooptic material, the permittivity tensor is modified by adding imaginary off-diagonal elements, in which case $\boldsymbol{\epsilon}$ cannot be diagonalized by a simple rotation.

Manuscript received September 25, 2007; revised January 4, 2008. This work was supported in part by the National Science Foundation (NSF) under CAREER Grant 0546928.

A. B. Fallahkhair and T. E. Murphy are with the Department of Electrical and Computer Engineering, University of Maryland, College Park, MD 20742 USA (e-mail: a.b.fallah@gmail.com; tem@umd.edu).

K. S. Li is with the Department of Computer Science and Electrical Engineering, New Jersey Institute of Technology, Newark, NJ 07102 USA (e-mail: ksl3@njit.edu).

Color versions of one or more of the figures in this paper are available online at http://ieeexplore.ieee.org.

Digital Object Identifier 10.1109/JLT.2008.923643

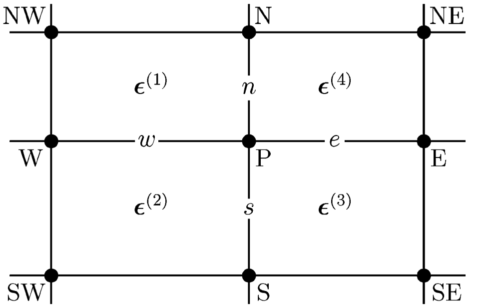

Fig. 1. Diagram illustrating mesh points used in the finite difference equations [14]. The superscripts P, N, S, E, W, NW, NE, SW, SE are used to label the point under consideration and its nearest neighbors to the north, south, east, west, northwest, northeast, southwest and southeast, respectively. The quantities n, s, e, and w denote the distance between P and the nearest mesh points in the north, south, west and east directions. The symbols $\boldsymbol{\epsilon}^{(1)} \ldots \boldsymbol{\epsilon}^{(4)}$ indicate the dielectric permittivity tensors, which are assumed to be homogeneous within each rectangular region between mesh points.

When the dielectric permittivity tensor is of the form given in (1), the vector eigenmode of the optical waveguide can be completely described by the two transverse magnetic field components H_x and H_y, from which all other electromagnetic field components can be derived [8].

The eigenvalue equation for the transverse magnetic fields can be obtained by combining both of Maxwell's curl equations [10]

$$\nabla \times (\boldsymbol{\epsilon}^{-1} \nabla \times \mathbf{H}) - \omega^2 \mu_0 \mathbf{H} = 0 \tag{2}$$

where we have assumed the material is nonmagnetic $(\mu = \mu_0)$ and all field quantities have a time dependence of $e^{j\omega t}$.

Assuming a z dependence of $e^{-j\beta z}$ for all fields, the longitudinal component H_z can be computed from the transverse components by applying the divergence relation $\nabla \cdot \mathbf{H} = 0$

$$H_z = \frac{1}{j\beta}\left(\frac{\partial H_x}{\partial x} + \frac{\partial H_y}{\partial y}\right). \tag{3}$$

Making use of (3), it is possible to express (2) entirely in terms of the two transverse magnetic field components. From the two transverse components of (2), one obtains, after some algebraic simplification, the following coupled eigenvalue equations for H_x and H_y

$$\begin{aligned} \frac{\partial^2 H_x}{\partial x^2} + \frac{\epsilon_{yy}}{\epsilon_{zz}}\frac{\partial^2 H_x}{\partial y^2} + \frac{\epsilon_{yx}}{\epsilon_{zz}}\frac{\partial^2 H_x}{\partial y \partial x} + \left(1 - \frac{\epsilon_{yy}}{\epsilon_{zz}}\right)\frac{\partial^2 H_y}{\partial x \partial y} & \\ - \frac{\epsilon_{yx}}{\epsilon_{zz}}\frac{\partial^2 H_y}{\partial x^2} + k^2(\epsilon_{yy} H_x - \epsilon_{yx} H_y) = \beta^2 H_x & \qquad \text{(4a)} \\ \frac{\partial^2 H_y}{\partial y^2} + \frac{\epsilon_{xx}}{\epsilon_{zz}}\frac{\partial^2 H_y}{\partial x^2} + \frac{\epsilon_{xy}}{\epsilon_{zz}}\frac{\partial^2 H_y}{\partial x \partial y} + \left(1 - \frac{\epsilon_{xx}}{\epsilon_{zz}}\right)\frac{\partial^2 H_x}{\partial y \partial x} & \\ - \frac{\epsilon_{xy}}{\epsilon_{zz}}\frac{\partial^2 H_x}{\partial y^2} + k^2(\epsilon_{xx} H_y - \epsilon_{xy} H_x) = \beta^2 H_y & \qquad \text{(4b)} \end{aligned}$$

where $k^2 \equiv \omega^2 \mu_0 \epsilon_0$.

Once all three components of $\mathbf{H}$ are known, $\mathbf{D}$ can be found by applying $\nabla \times \mathbf{H} = j\omega \mathbf{D}$, which gives

$$\begin{aligned} D_x &= -\frac{1}{\omega\beta}\left(\frac{\partial^2 H_x}{\partial y \partial x} + \frac{\partial^2 H_y}{\partial y^2}\right) + \frac{\beta}{\omega} H_y \\ D_y &= +\frac{1}{\omega\beta}\left(\frac{\partial^2 H_y}{\partial x \partial y} + \frac{\partial^2 H_x}{\partial x^2}\right) - \frac{\beta}{\omega} H_x \\ D_z &= \frac{j}{\omega}\left(\frac{\partial H_x}{\partial y} - \frac{\partial H_y}{\partial x}\right) \end{aligned} \tag{5}$$

and the electric field can be computed from $\mathbf{D}$ by using $\mathbf{E} = \boldsymbol{\epsilon}^{-1}\mathbf{D}$

$$\begin{bmatrix} E_x \\ E_y \end{bmatrix} = \frac{1}{\epsilon_0(\epsilon_{xx}\epsilon_{yy} - \epsilon_{xy}\epsilon_{yx})} \begin{bmatrix} \epsilon_{yy} & -\epsilon_{xy} \\ -\epsilon_{yx} & \epsilon_{xx} \end{bmatrix} \begin{bmatrix} D_x \\ D_y \end{bmatrix} \tag{6}$$

$$E_z = \frac{1}{\epsilon_0 \epsilon_{zz}} D_z = \frac{j}{\omega \epsilon_0 \epsilon_{zz}}\left(\frac{\partial H_x}{\partial y} - \frac{\partial H_y}{\partial x}\right). \tag{7}$$

The coupled eigenmode (4a), (4b) can be collected into a single vector equation of the form

$$\begin{bmatrix} A_{xx} & A_{xy} \\ A_{yx} & A_{yy} \end{bmatrix} \begin{bmatrix} H_x \\ H_y \end{bmatrix} = \beta^2 \begin{bmatrix} H_x \\ H_y \end{bmatrix} \tag{8}$$

where A_{jk} are differential operators to be approximated using finite difference methods. When deriving the finite difference equations, we assume that the dielectric tensor $\boldsymbol{\epsilon}$ is piecewise uniform, with boundaries constrained to coincide with the finite difference grid points, as depicted in Fig. 1. The spacing between mesh points need not be uniform, and can even be complex should one wish to incorporate perfectly-matched layers using the complex coordinate stretching method [21]. The finite difference operators representing A_{xx} and A_{xy} can be expressed in terms of the transverse magnetic fields at the point under consideration (P) and at the eight neighboring grid points

$$\begin{aligned} & a_{xx}^{(\mathrm{NW})} H_x^{(\mathrm{NW})} + a_{xx}^{(\mathrm{N})} H_x^{(\mathrm{N})} + a_{xx}^{(\mathrm{NE})} H_x^{(\mathrm{NE})} + a_{xx}^{(\mathrm{W})} H_x^{(\mathrm{W})} \\ & \quad + a_{xx}^{(\mathrm{P})} H_x^{(\mathrm{P})} + a_{xx}^{(\mathrm{E})} H_x^{(\mathrm{E})} + a_{xx}^{(\mathrm{SW})} H_x^{(\mathrm{SW})} + a_{xx}^{(\mathrm{S})} H_x^{(\mathrm{S})} \\ & \quad + a_{xx}^{(\mathrm{SE})} H_x^{(\mathrm{SE})} + a_{xy}^{(\mathrm{NW})} H_y^{(\mathrm{NW})} + a_{xy}^{(\mathrm{N})} H_y^{(\mathrm{N})} \\ & \quad + a_{xy}^{(\mathrm{NE})} H_y^{(\mathrm{NE})} + a_{xy}^{(\mathrm{W})} H_y^{(\mathrm{W})} + a_{xy}^{(\mathrm{P})} H_y^{(\mathrm{P})} \\ & \quad + a_{xy}^{(\mathrm{E})} H_y^{(\mathrm{E})} + a_{xy}^{(\mathrm{SW})} H_y^{(\mathrm{SW})} + a_{xy}^{(\mathrm{S})} H_y^{(\mathrm{S})} + a_{xy}^{(\mathrm{SE})} H_y^{(\mathrm{SE})} \\ & \quad = \beta^2 H_x^{(\mathrm{P})} \end{aligned} \tag{9}$$

and similarly for A_{yx} and A_{yy}

$$\begin{aligned} & a_{yx}^{(\mathrm{NW})} H_x^{(\mathrm{NW})} + a_{yx}^{(\mathrm{N})} H_x^{(\mathrm{N})} + a_{yx}^{(\mathrm{NE})} H_x^{(\mathrm{NE})} + a_{yx}^{(\mathrm{W})} H_x^{(\mathrm{W})} \\ & \quad + a_{yx}^{(\mathrm{P})} H_x^{(\mathrm{P})} + a_{yx}^{(\mathrm{E})} H_x^{(\mathrm{E})} + a_{yx}^{(\mathrm{SW})} H_x^{(\mathrm{SW})} + a_{yx}^{(\mathrm{S})} H_x^{(\mathrm{S})} \\ & \quad + a_{yx}^{(\mathrm{SE})} H_x^{(\mathrm{SE})} + a_{yy}^{(\mathrm{NW})} H_y^{(\mathrm{NW})} + a_{yy}^{(\mathrm{N})} H_y^{(\mathrm{N})} \\ & \quad + a_{yy}^{(\mathrm{NE})} H_y^{(\mathrm{NE})} + a_{yy}^{(\mathrm{W})} H_y^{(\mathrm{W})} + a_{yy}^{(\mathrm{P})} H_y^{(\mathrm{P})} + a_{yy}^{(\mathrm{E})} H_y^{(\mathrm{E})} \\ & \quad + a_{yy}^{(\mathrm{SW})} H_y^{(\mathrm{SW})} + a_{yy}^{(\mathrm{S})} H_y^{(\mathrm{S})} + a_{yy}^{(\mathrm{SE})} H_y^{(\mathrm{SE})} \\ & \quad = \beta^2 H_y^{(\mathrm{P})}. \end{aligned} \tag{10}$$

The expressions for the finite difference coefficients a_{jk} are summarized in the Appendix. Using these equations, each of the operators A_{xx}, A_{xy}, A_{yx}, A_{yy} can be replaced by a $N \times N$ sparse matrix, where $N \equiv (n_x + 1)(n_y + 1)$. When these four sparse matrices are assembled as in (8), the eigenvectors and eigenvalues of the resulting matrix give the modes and propagation constants of the waveguide.

Fig. 2 illustrates the form of the sparse matrix $\mathbf{A}$ for a small computational window with $n_x = 4$ and $n_y = 2$ filled with a homogeneous dielectric material. In this example, each of the

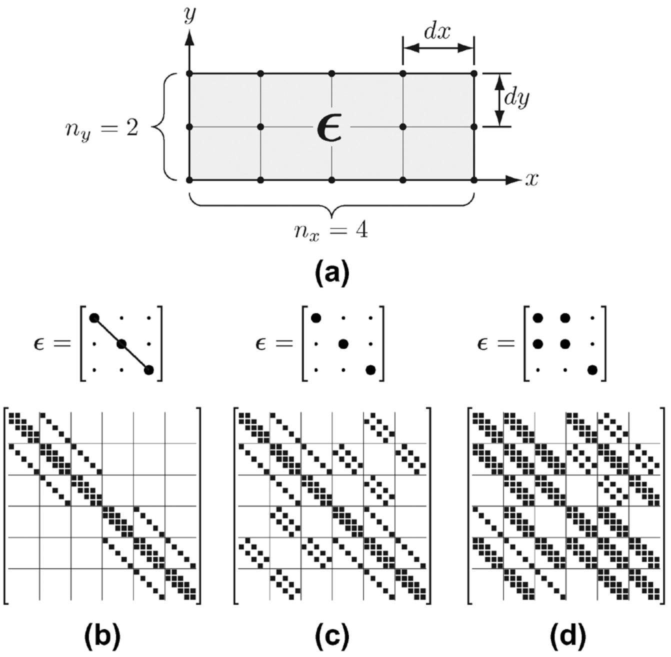

Fig. 2. (a) Small computational window with $n_x + 1 = 5$ and $n_y + 1 = 3$ filled with a homogeneous optical material. (b) Sparsity structure of the corresponding matrix $\mathbf{A}$ when the entire computational window is filled with an isotropic material. Each row has only 5 nonzero matrix elements. (Note that in the absence of edges or inhomogeneities, H_x and H_y are decoupled.) (c) When the dielectric permittivity is anisotropic, but diagonal, the number of nonzero elements per row grows to 9. (d) When the dielectric permittivity is anisotropic and nondiagonal, as in (1), there are 16 nonzero elements per row.

four sub-matrices A_{ij} is a 15 × 15 matrix. When the dielectric material is isotropic and homogeneous, A_{xx} and A_{yy} reduce to the standard 5-point finite difference operators, as depicted in Fig. 2(b). If the dielectric permittivity is anisotropic, but still diagonal, the number of nonzero matrix elements per row increases from 5 to 9, as shown in Fig. 2(c). For an anisotropic material with nondiagonal permittivity, there are 16 nonzero matrix elements in each interior row of $\mathbf{A}$, as shown in Fig. 2(d). In a typical waveguide problem, only a portion of the computational window would be filled with anisotropic or nondiagonal materials, in which case the memory requirements could be estimated by performing a suitable weighted summation.

The calculations described in the following section were performed on a personal computer with an Intel Core 2 Duo CPU, with 2 GB of physical RAM (approximately 1.2 GB available after startup). Under these conditions, the maximum problem size was limited to sparse matrices with fewer than approximately 2.8 million nonzero elements for real matrices and 1.4 million nonzero elements for matrices that contain complex elements. All simulations could be completed in less than 60 s.

III. EXAMPLES

A. *Magnetooptical Channel Waveguide*

To demonstrate the capabilities of the anisotropic modesolver, we computed the eigenmodes of the magnetooptical channel waveguide depicted in Fig. 3 [22]. The gadolinium gallium garnet (GGG) lower cladding layer was assumed to be isotropic, with a refractive index of $n_1 = 1.95$, and the top cladding layer was taken to be air $(n_3 = 1)$. The yttrium iron garnet (YIG) core layer was described by a relative permittivity tensor of

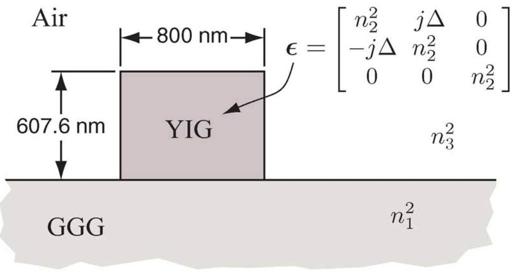

Fig. 3. Diagram of magneto-optical channel waveguide comprised of a yttrium iron garnet (YIG) core over a gadolinium gallium garnet (GGG) substrate [22]. The substrate is assumed to be isotropic, while the YIG layer is taken to be magneto-optical.

$$\begin{bmatrix} n_2^2 & +j\Delta & \\ -j\Delta & n_2^2 & 0 \\ 0 & 0 & n_2^2 \end{bmatrix} \tag{11}$$

where $n_2 = 2.302$ and $\Delta = 0.005$, which would produce Faraday rotation at a rate of $3000^\circ/\mathrm{cm}$ in a bulk material. All calculations were performed assuming a vacuum wavelength of 1300 nm, and the waveguide dimensions depicted in Fig. 3. The core thickness was carefully adjusted in order to make the quasi-TE and quasi-TM modes nearly degenerate when $\Delta = 0$.

The mode calculations were performed over a $3.2\ \mu\mathrm{m} \times 2.9\ \mu\mathrm{m}$ window, divided into 320 × 348 $(n_x \times n_y)$ regions. The grid spacing was 6.25 nm in the horizontal direction and 4.9 nm in the vertical direction, but the grid spacing was parabolically stretched in the cladding regions in order to reach the edges of the computation window.

The eigenmodes of the waveguide were calculated using an iterative shift-invert sparse matrix eigenvector solver (ARPACK [23]) provided through a built-in MATLAB function (eigs.) This routine uses an iterative Lanczos method to compute the largest eigenvalues and corresponding eigenvectors of the shifted matrix $(\mathbf{A} - \sigma\mathbf{I})^{-1}$, and a sparse matrix solver (UMFPACK [24]) to perform the matrix multiplication $\mathbf{v} = (\mathbf{A} - \sigma\mathbf{I})^{-1}\mathbf{u}$ at each step.

Both of calculated modes exhibit complex transverse magnetic field components H_x and H_y that are nearly equal in magnitude, but out of phase by $\pm\pi/2$, indicating that the modes are circularly polarized. To illustrate this, Fig. 4 plots the field components $H_\pm \equiv (H_x \pm jH_y)/\sqrt{2}$ for the first two modes. For the first mode, the component H_- is suppressed by at least 17 dB relative to the peak value of $\mathbf{H}$, indicating that we may approximate $H_x \simeq jH_y$, i.e., the first mode is left-hand circularly polarized. By a similar argument, the second-mode exhibits a right-hand circular polarization state.

It is notable that although the finite difference matrix $\mathbf{A}$ is both complex and non-Hermitian for this problem, both of the computed eigenvalues were real, as expected for a lossless waveguide.

The calculated effective indices for the two circularly-polarized modes shown in Fig. 4 are $n_{\text{eff}}^{(1)} = 2.048795$ and $n_{\text{eff}}^{(2)} =$

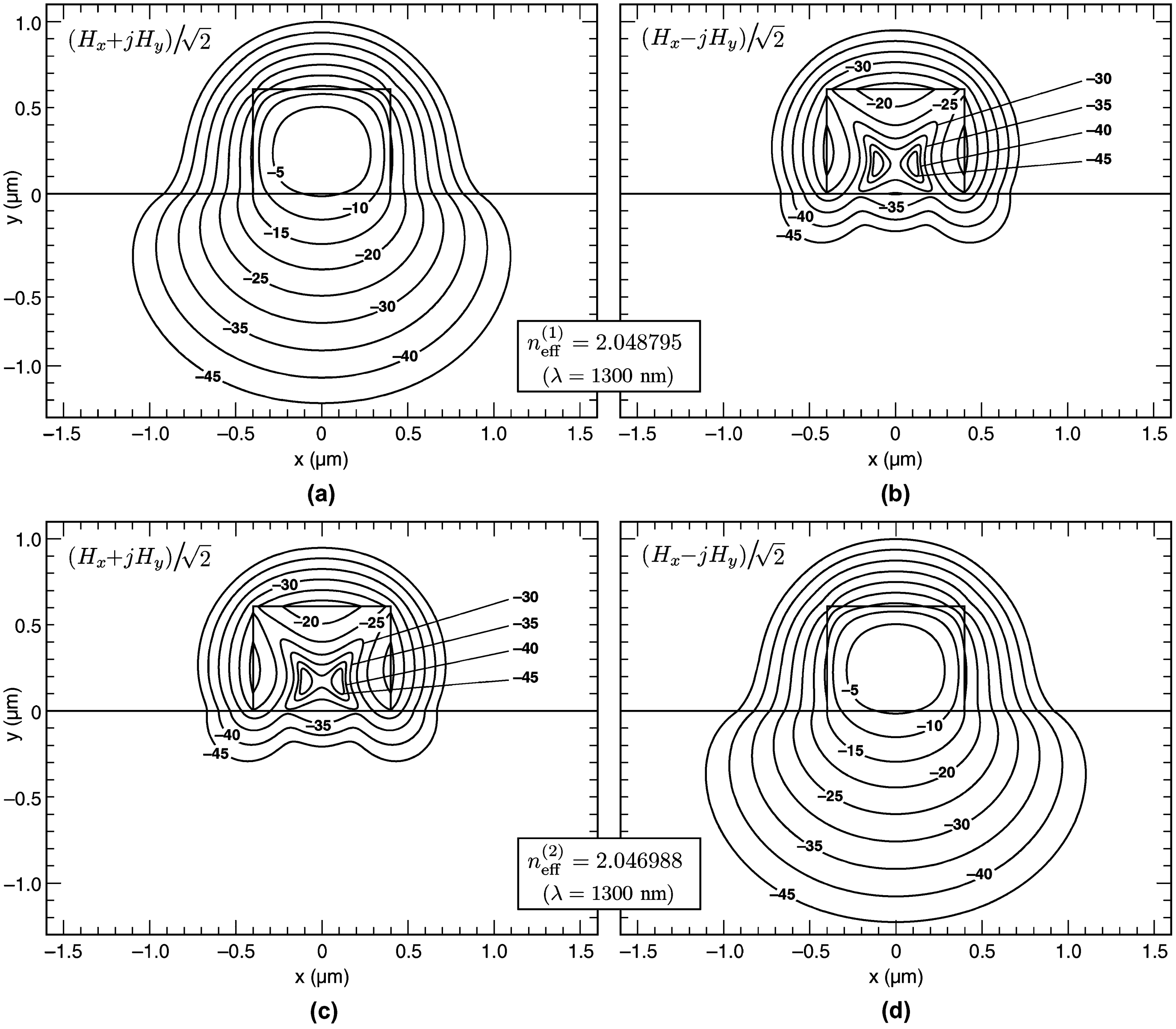

(a) (b)

(c) (d)

Fig. 4. Transverse magnetic fields of the first two eigenmodes modes of a magneto-optic waveguide, calculated at a free-space wavelength of 1300 nm. To better illustrate the circular polarization states the modes, the combinations $H_{\pm} = (H_x \pm jH_y)/\sqrt{2}$ are plotted for each mode. The contour labels indicate the magnitude of the field in dB, relative to the peak transverse magnetic field of each mode. (a),(b) In the fundamental mode, the combination $(H_x - jH_y)/\sqrt{2}$ is suppressed relative to the peak field, indicating that the mode is primarily left-hand circular polarized. (c),(d) In the second-order mode, the combination $(H_x + jH_y)/\sqrt{2}$ is suppressed, indicating a right-hand circular polarization.

2.046988. The corresponding effective modal Faraday rotation rate is then found to be

$$\Theta_F^{(\rm eff)} = \frac{\pi}{\lambda}\left(n_{\rm eff}^{(1)} - n_{\rm eff}^{(2)}\right) = 2502^\circ/\text{cm}. \tag{12}$$

This result is smaller than that of the constituent YIG core layer because a portion of the mode intensity resides in the nonmagnetooptic cladding.

In this example, the off-diagonal elements of the permittivity tensor are small compared to the index difference between the core and cladding layers of the waveguide. It is therefore also reasonable to model the anisotropy using coupled mode theory (CMT) [25], in which the imaginary off-diagonal terms are treated as a small perturbation of an otherwise isotropic waveguide. In this case, vector coupled mode theory yields the following expression for the approximate propagation constants [26]:

$$\beta = \frac{\beta_{\rm TE} + \beta_{\rm TM}}{2} \pm \left[\left(\frac{\beta_{\rm TE} - \beta_{\rm TM}}{2}\right)^2 + |\kappa|^2\right]^{1/2} \tag{13}$$

where $\beta_{\rm TE}$ and $\beta_{\rm TM}$ are the propagation constants of the quasi-TE and quasi-TM modes of the unperturbed (isotropic)

TABLE I
COUPLED MODE THEORY VERSUS EXACT EIGENMODES

	Coupled Mode Theory[a]		Exact[b]	
Δ	$n_{\text{eff}}^{(1)}$	$n_{\text{eff}}^{(2)}$	$n_{\text{eff}}^{(1)}$	$n_{\text{eff}}^{(2)}$
0.0001	2.047909	2.047873	2.047909	2.047873
0.0002	2.047927	2.047856	2.047927	2.047855
0.0005	2.047980	2.047803	2.047982	2.047801
0.0010	2.048068	2.047714	2.048072	2.047710
0.0020	2.048246	2.047537	2.048253	2.047530
0.0050	2.048777	2.047005	2.048795	2.046988

[a] The unperturbed modes were calculated using the full-vector modesolver with isotropic materials. The unperturbed refractive indices are found to be $n_{\text{TE}} = 2.047889$ and $n_{\text{TE}} = 2.047893$. Calculations were performed over a 3.2×2.9 μm computational window with 320 × 348 gridpoints and a minimum grid size of 6.25 × 4.9 nm.

[b] The "exact" eigenmodes were calculated using the full-vector anisotropic modesolver with imaginary off-diagonal terms. The computational window and grid spacing were identical to that used in the CMT calculations.

waveguide. κ is an overlap integral involving the two eigenmodes

$$\kappa = \frac{\omega\epsilon_0}{4\sqrt{P_{\text{TE}}P_{\text{TM}}}} \int\!\!\int \mathbf{E}_{\text{TE}}^{*} \cdot (\boldsymbol{\Delta\epsilon} \cdot \mathbf{E}_{\text{TM}}) dA \qquad (14)$$

where P_{TE} denotes the total power of the TE eigenmode

$$P_{\text{TE}} = \frac{1}{4} \int\!\!\int (\mathbf{E}_{\text{TE}} \times \mathbf{H}_{\text{TE}}^{*} + \mathbf{E}_{\text{TE}}^{*} \times \mathbf{H}_{\text{TE}}) \cdot \mathbf{dA} \qquad (15)$$

and P_{TM} is similarly defined. For the magnetooptical waveguide considered here, $\boldsymbol{\Delta}\epsilon$ is zero everywhere except within of the core region where it is given by

$$\boldsymbol{\Delta\epsilon} = \begin{bmatrix} 0 & j\Delta & 0 \\ -j\Delta & 0 & 0 \\ 0 & 0 & 0 \end{bmatrix}. \qquad (16)$$

Table I compares the propagation constants calculated using coupled mode theory to those obtained by directly calculating the exact eigenmodes of the anisotropic structure, for six different values of Δ. For the CMT calculations, the transverse field components $\mathbf{H}_x$ and $\mathbf{H}_y$ were first calculated for the eigenmodes of unperturbed isotropic waveguide using a finite difference mesh identical to that used in the anisotropic case. The transverse electric field components were then calculated numerically using (5), and the integrals in (14) and (15) were approximated by a two-dimensional Reimann summation.

When $\Delta = 0.0001$, the coupled mode theory and exact eigenmode solutions are in perfect agreement (to within 6 decimal places). As Δ is increased to 0.005, there is a small, but numerically significant discrepancy between the two results. Nonetheless, even for the strongest magnetooptical materials, the accuracy of vector-CMT is adequate for many design problems.

For the computational mesh considered in this example, the sparse matrix $\mathbf{A}$ representing the isotropic waveguide has 1 119 958 real nonzero elements compared to 1 342 180 complex elements for the anisotropic waveguide. These numbers average to 5 real nonzero matrix elements per row for the isotropic case compared to 6.0 complex elements per row for the anisotropic nondiagonal case. Because the isotropic finite difference operator requires less memory and computational resources than the anisotropic operator, the coupled-mode approach would allow one to use a finer mesh discretization for the same computational expense and memory utilization.

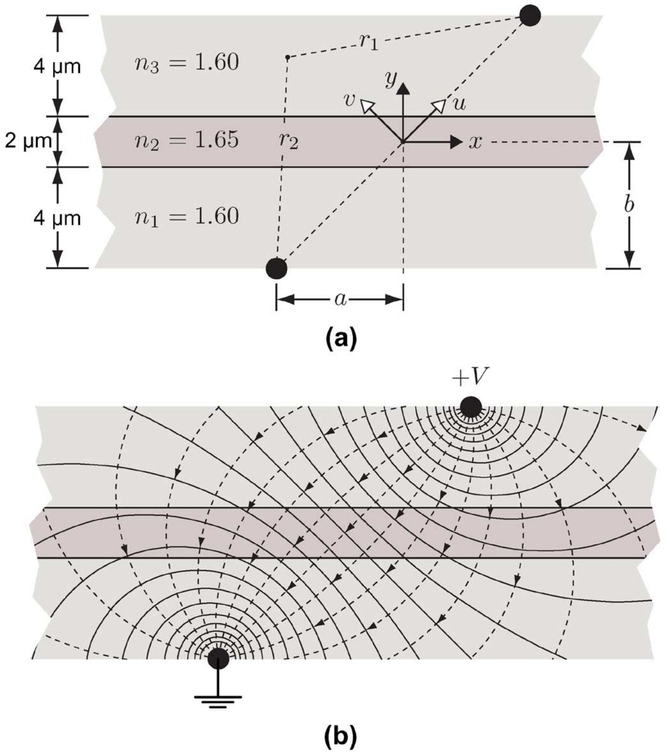

Fig. 5. (a) Diagram of a poling-induced polymer electrooptic waveguide. The central core layer becomes positive uniaxial in the direction of the applied field when the structure is poled by the electrodes placed above and below the waveguide. For simplicity, we approximate the poling potential and electric field as that of two thin wires located at $(x, y) = (\pm a, \pm b)$. (b) Contour plot of electromagnetic poling potential (solid lines) and the associated electric field lines (dashed).

B. Poling-Induced Polymer Waveguide

As a second example, we consider the eigenmodes of an electrooptic polymer waveguide that is poled at an oblique angle relative to the y direction, as shown in Fig. 5. Such devices find applications in mode converters, circular polarization modulators, and polarization-independent modulators [20], [27]–[29]. In this waveguide, the three dielectric layers provide confinement in the vertical direction, while horizontal confinement is provided entirely by the anisotropy produced in the middle layer when the device is poled. The cladding layers are assumed to be nonpolar (and hence immune to the poling field) with an isotropic refractive index of $n_1 = n_3 = 1.60$. The middle layer is modeled as an electrooptic polymer with a refractive index of $n_2 = 1.65$ prior to poling.

This waveguide structure provides an interesting challenge for mode calculations because both the orientation and strength of the birefringence are nonuniform throughout the waveguide core. Moreover, the induced anisotropy, although small, plays an essential role in guaranteeing transverse mode confinement.

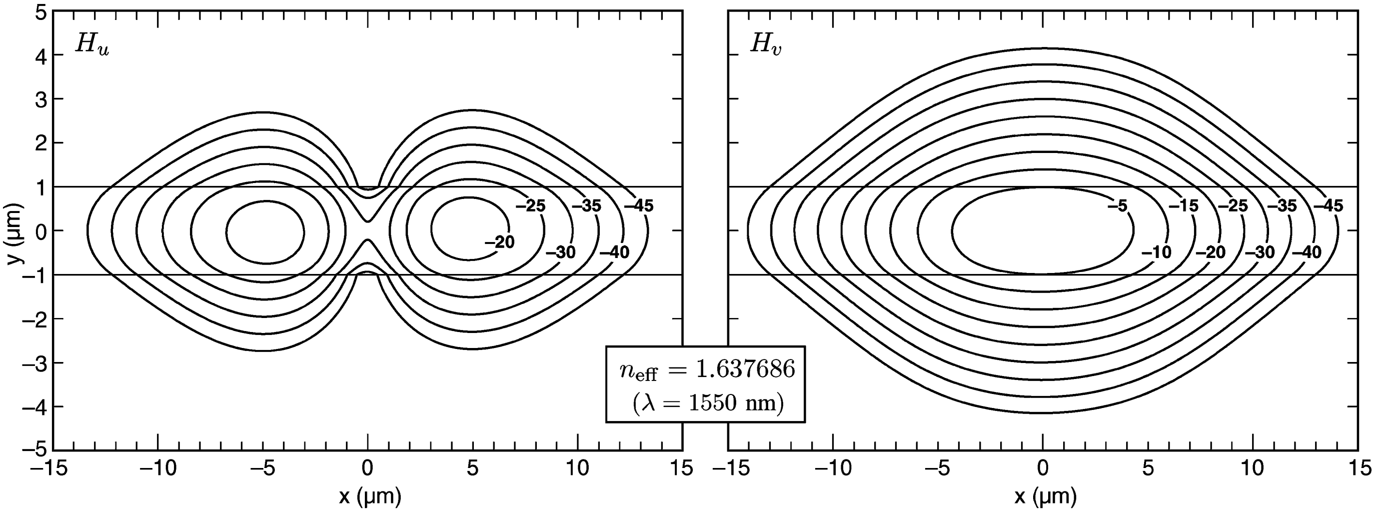

(a) **(b)**

Fig. 6. Calculated transverse magnetic field components H_u and H_v of the fundamental mode of a poling-induced polymer waveguide. The peak value of H_u component is more than −17 dB lower than the peak value of H_v, indicating that the transverse magnetic field is mostly polarized along the direction perpendicular to the axis between the poling electrodes. The contour labels indicate the magnitude of the field, relative to the peak vector amplitude. The mode is calculated at a free-space wavelength of 1550 nm.

In contrast to the previous example, the anisotropy in this waveguide cannot be accurately modeled as a perturbation of an otherwise isotropic or even diagonal anisotropic waveguide.

Although an accurate analysis would require one to numerically compute the electrostatic poling potential, here we make the simple assumption that the poling potential can be approximated as that of two thin wires located symmetrically at $(x, y) = (\pm a, \pm b)$ in a homogeneous dielectric. Under this assumption, the poling potential is

$$V(x, y) = E_0 \frac{\sqrt{a^2 + b^2}}{4} \ln \left(\frac{r_2(x, y)}{r_1(x, y)} \right) \tag{17}$$

where E_0 describes the magnitude of the electric field at $x = y = 0$ and r_1 and r_2 are the geometrical distances from the point (x, y) to the two poling electrodes, as depicted in Fig. 5(a).

The poling induces a uniaxial positive inhomogeneous birefringence Δn within the core layer that is proportional to the electrostatic field intensity $|\mathbf{E}|^2$, with the axis of anisotropy oriented in the direction of the poling field. Fig. 5(b) illustrates the electrostatic potential and associated field lines for the twin-wire electrode configuration considered here. For the electric potential described by (17), the induced birefringence in the middle layer is calculated to be

$$\Delta n(x, y) = \delta_0 \left(\frac{a^2 + b^2}{r_1(x, y) r_2(x, y)} \right)^2 \tag{18}$$

where δ_0 denotes the birefringence at $x = y = 0$, which is proportional to E_0^2. The axis of anisotropy is oriented at an angle $\theta(x, y)$, given by

$$\tan \theta(x, y) = \frac{b(x^2 - y^2 + a^2 + b^2) - 2axy}{a(y^2 - x^2 + a^2 + b^2) - 2bxy}. \tag{19}$$

The net birefringence is assumed to be split between the ordinary and extraordinary indices in the following way [20], [30]:

$$n_{2e} = n_2 + \frac{2}{3} \Delta n, \quad n_{2o} = n_2 - \frac{1}{3} \Delta n \tag{20}$$

with Δn given by (18). The local permittivity tensor in the middle layer is then described by

$$\begin{bmatrix} n_{2e}^2 \cos^2 \theta + n_{2o}^2 \sin^2 \theta & \left(n_{2e}^2 - n_{2o}^2\right) \sin \theta \cos \theta & 0 \\ \left(n_{2e}^2 - n_{2o}^2\right) \sin \theta \cos \theta & n_{2o}^2 \cos^2 \theta + n_{2e}^2 \sin^2 \theta & 0 \\ 0 & 0 & n_{2o}^2 \end{bmatrix}$$

with θ given by (19).

Because the induced ordinary refractive index is smaller than the unpoled index, the waveguide supports only one polarization state.

The fundamental eigenmode was calculated using 600 × 300 grid points distributed over a 40×10 μm computational window with a minimum grid size of 50 × 33.3 nm. The horizontal grid size was parabolically stretched near the east and west edges of the computational window. When calculating the anisotropy, we used $a = b = 5$ μm and $\delta_0 = 0.01$.

The effective index of the fundamental eigenmode was calculated to be 1.637686, and the corresponding transverse magnetic field components are plotted in Fig. 6. In order to better convey the polarization state of this mode, instead of plotting $\mathbf{H}_x$ and $\mathbf{H}_y$ we have instead constructed the field components $\mathbf{H}_u$ and $\mathbf{H}_v$, where u indicates the direction measured along the axis connecting the two electrodes and v indicates the orthogonal direction, as labeled in Fig. 5(a).

Although the direction of the transverse magnetic field is not homogeneous for this mode, the component $\mathbf{H}_v$ remains significantly larger than $\mathbf{H}_u$, especially near the center of the mode, indicating that the prevailing direction of the magnetic field is perpendicular to the axis between the electrodes. The corresponding electric field would therefore be primarily polarized along the axis between the poling electrodes, as expected for a positive uniaxial poled material.

IV. CONCLUSION

We describe a versatile finite difference operator for computing the eigenmodes of anisotropic dielectric waveguides. The method computes the two transverse magnetic field components H_x and H_y for dielectric waveguides comprised of materials with arbitrary transverse anisotropy, i.e., materials that are symmetric under the reflection $z \to -z$. Even though the calculated finite difference matrix is non-Hermitian and in some cases complex, in all of the cases considered it yields real propagation constants (eigenvalues) as long as the constituent materials are lossless. The technique is used to analyze the eigenmodes of an off-axis poled polymer waveguide and the left and right circularly-polarized modes of a waveguide Faraday rotator. The reported approach could enable more accurate modeling of a variety of integrated optical components including polarizers, polarization rotators, isolators, mode converters, polarization splitters, and electrooptic modulators.

APPENDIX
FINITE DIFFERENCE COEFFICIENTS

The finite difference equations representing (4a) and (4b) are derived using a method analogous to that described in [16], [18]. The partial derivatives that appear in (4a) and (4b) are approximated by a two-dimensional second-order Taylor series expansion of H_x and H_y about the point P, in each of the four quadrants. The solutions in the four quadrants are then connected by enforcing the continuity of H_z and E_z at the boundaries.

When discretizing (4a), the continuity of E_z is applied first at the boundary between regions 1 and 2, and again at the interface between regions 3 and 4. The resulting two equations are combined to eliminate terms involving $\partial H_x/\partial x$, while using a standard central difference equation to approximate $\partial H_y/\partial x$. After algebraic simplification, this procedure yields the following finite difference coefficients representing A_{xx} and A_{xy}

$$a_{xx}^{(\mathrm{N})} = \frac{\epsilon_{yy}^{(3)}}{\epsilon_{zz}^{(4)}} \frac{2e\epsilon_{yy}^{(4)} - n\epsilon_{yx}^{(4)}}{v_{34} n(e+w)} + \frac{\epsilon_{yy}^{(2)}}{\epsilon_{zz}^{(1)}} \frac{2w\epsilon_{yy}^{(1)} + n\epsilon_{yx}^{(1)}}{v_{21} n(e+w)} \tag{21}$$

$$a_{xx}^{(\mathrm{S})} = \frac{\epsilon_{yy}^{(4)}}{\epsilon_{zz}^{(3)}} \frac{2e\epsilon_{yy}^{(3)} - s\epsilon_{yx}^{(3)}}{v_{34} s(e+w)} + \frac{\epsilon_{yy}^{(1)}}{\epsilon_{zz}^{(2)}} \frac{2w\epsilon_{yy}^{(2)} + s\epsilon_{yx}^{(2)}}{v_{21} s(e+w)} \tag{22}$$

$$a_{xx}^{(\mathrm{E})} = \frac{2}{e(e+w)} + \frac{\epsilon_{yy}^{(4)}\epsilon_{yx}^{(3)}/\epsilon_{zz}^{(3)} - \epsilon_{yy}^{(3)}\epsilon_{yx}^{(4)}/\epsilon_{zz}^{(4)}}{v_{34}(e+w)} \tag{23}$$

$$a_{xx}^{(\mathrm{W})} = \frac{2}{w(e+w)} + \frac{\epsilon_{yy}^{(2)}\epsilon_{yx}^{(1)}/\epsilon_{zz}^{(1)} - \epsilon_{yy}^{(1)}\epsilon_{yx}^{(2)}/\epsilon_{zz}^{(2)}}{v_{21}(e+w)} \tag{24}$$

$$a_{xx}^{(\mathrm{NE})} = \frac{\epsilon_{yx}^{(4)}\epsilon_{yy}^{(3)}}{\epsilon_{zz}^{(4)} v_{34}(e+w)}, \quad a_{xx}^{(\mathrm{SE})} = \frac{-\epsilon_{yx}^{(3)}\epsilon_{yy}^{(4)}}{\epsilon_{zz}^{(3)} v_{34}(e+w)} \tag{25}$$

$$a_{xx}^{(\mathrm{SW})} = \frac{\epsilon_{yx}^{(2)}\epsilon_{yy}^{(1)}}{\epsilon_{zz}^{(2)} v_{21}(e+w)}, \quad a_{xx}^{(\mathrm{NW})} = \frac{-\epsilon_{yx}^{(1)}\epsilon_{yy}^{(2)}}{\epsilon_{zz}^{(1)} v_{21}(e+w)} \tag{26}$$

$$\begin{aligned} a_{xx}^{(\mathrm{P})} = & - a_{xx}^{(\mathrm{N})} - a_{xx}^{(\mathrm{S})} - a_{xx}^{(\mathrm{E})} - a_{xx}^{(\mathrm{W})} - a_{xx}^{(\mathrm{NE})} \\ & - a_{xx}^{(\mathrm{SE})} - a_{xx}^{(\mathrm{SW})} - a_{xx}^{(\mathrm{NW})} \\ & + k^2 \frac{n+s}{e+w} \left(\epsilon_{yy}^{(4)}\epsilon_{yy}^{(3)} \frac{e}{v_{34}} + \epsilon_{yy}^{(1)}\epsilon_{yy}^{(2)} \frac{w}{v_{21}} \right) \end{aligned} \tag{27}$$

$$a_{xy}^{(\mathrm{N})} = \frac{\dfrac{s\epsilon_{yy}^{(2)}\epsilon_{yy}^{(4)}}{v_{21}v_{34}} - \dfrac{s\epsilon_{yy}^{(1)}\epsilon_{yy}^{(3)}}{v_{21}v_{34}} + \dfrac{\epsilon_{yy}^{(3)}\epsilon_{yy}^{(4)}}{\epsilon_{zz}^{(4)} v_{34}} - \dfrac{\epsilon_{yy}^{(2)}\epsilon_{yy}^{(1)}}{\epsilon_{zz}^{(1)} v_{21}}}{(e+w)} \tag{28}$$

$$a_{xy}^{(\mathrm{S})} = \frac{\dfrac{n\epsilon_{yy}^{(2)}\epsilon_{yy}^{(4)}}{v_{21}v_{34}} - \dfrac{n\epsilon_{yy}^{(1)}\epsilon_{yy}^{(3)}}{v_{21}v_{34}} + \dfrac{\epsilon_{yy}^{(1)}\epsilon_{yy}^{(2)}}{\epsilon_{zz}^{(2)} v_{21}} - \dfrac{\epsilon_{yy}^{(4)}\epsilon_{yy}^{(3)}}{\epsilon_{zz}^{(3)} v_{34}}}{(e+w)} \tag{29}$$

$$\begin{aligned} a_{xy}^{(\mathrm{E})} = & \frac{\epsilon_{yy}^{(4)}\left(1 - \epsilon_{yy}^{(3)}/\epsilon_{zz}^{(3)}\right) - \epsilon_{yy}^{(3)}\left(1 - \epsilon_{yy}^{(4)}/\epsilon_{zz}^{(4)}\right)}{v_{34}(e+w)} - \frac{2}{e(e+w)^2} \\ & \times \left[\frac{nw\epsilon_{yx}^{(1)}\epsilon_{yy}^{(2)}}{\epsilon_{zz}^{(1)} v_{21}} + \frac{sw\epsilon_{yx}^{(2)}\epsilon_{yy}^{(1)}}{\epsilon_{zz}^{(2)} v_{21}} + \frac{ne\epsilon_{yx}^{(4)}\epsilon_{yy}^{(3)}}{\epsilon_{zz}^{(4)} v_{34}} \right. \\ & + \frac{se\epsilon_{yx}^{(3)}\epsilon_{yy}^{(4)}}{\epsilon_{zz}^{(3)} v_{34}} + \frac{w^2\epsilon_{yy}^{(1)}\epsilon_{yy}^{(2)}}{v_{21}} \left(\frac{1}{\epsilon_{zz}^{(1)}} - \frac{1}{\epsilon_{zz}^{(2)}} \right) \\ & \left. + \frac{ew\epsilon_{yy}^{(3)}\epsilon_{yy}^{(4)}}{v_{34}} \left(\frac{1}{\epsilon_{zz}^{(4)}} - \frac{1}{\epsilon_{zz}^{(3)}} \right) \right] \end{aligned} \tag{30}$$

$$\begin{aligned} a_{xy}^{(\mathrm{W})} = & \frac{\epsilon_{yy}^{(2)}(1 - \epsilon_{yy}^{(1)}/\epsilon_{zz}^{(1)}) - \epsilon_{yy}^{(1)}\left(1 - \epsilon_{yy}^{(2)}/\epsilon_{zz}^{(2)}\right)}{v_{21}(e+w)} - \frac{2}{w(e+w)^2} \\ & \times \left[\frac{ne\epsilon_{yx}^{(4)}\epsilon_{yy}^{(3)}}{\epsilon_{zz}^{(4)} v_{34}} + \frac{se\epsilon_{yx}^{(3)}\epsilon_{yy}^{(4)}}{\epsilon_{zz}^{(3)} v_{34}} + \frac{nw\epsilon_{yx}^{(1)}\epsilon_{yy}^{(2)}}{\epsilon_{zz}^{(1)} v_{21}} \right. \\ & + \frac{sw\epsilon_{yx}^{(2)}\epsilon_{yy}^{(1)}}{\epsilon_{zz}^{(2)} v_{21}} + \frac{e^2\epsilon_{yy}^{(4)}\epsilon_{yy}^{(3)}}{v_{34}} \left(\frac{1}{\epsilon_{zz}^{(3)}} - \frac{1}{\epsilon_{zz}^{(4)}} \right) \\ & \left. + \frac{ew\epsilon_{yy}^{(2)}\epsilon_{yy}^{(1)}}{v_{12}} \left(\frac{1}{\epsilon_{zz}^{(2)}} - \frac{1}{\epsilon_{zz}^{(1)}} \right) \right] \end{aligned} \tag{31}$$

$$a_{xy}^{(\mathrm{NE})} = \frac{\epsilon_{yy}^{(3)} - \dfrac{\epsilon_{yy}^{(3)}\epsilon_{yy}^{(4)}}{\epsilon_{zz}^{(4)}}}{v_{34}(e+w)}, \quad a_{xy}^{(\mathrm{SE})} = \frac{\dfrac{\epsilon_{yy}^{(4)}\epsilon_{yy}^{(3)}}{\epsilon_{zz}^{(3)}} - \epsilon_{yy}^{(4)}}{v_{34}(e+w)} \tag{32}$$

$$a_{xy}^{(\mathrm{NW})} = \frac{\dfrac{\epsilon_{yy}^{(2)}\epsilon_{yy}^{(1)}}{\epsilon_{zz}^{(1)}} - \epsilon_{yy}^{(2)}}{v_{21}(e+w)}, \quad a_{xy}^{(\mathrm{SW})} = \frac{\epsilon_{yy}^{(1)} - \dfrac{\epsilon_{yy}^{(1)}\epsilon_{yy}^{(2)}}{\epsilon_{zz}^{(2)}}}{v_{21}(e+w)} \tag{33}$$

$$\begin{aligned} a_{xy}^{(\mathrm{P})} = & - a_{xy}^{(\mathrm{N})} - a_{xy}^{(\mathrm{S})} - a_{xy}^{(\mathrm{E})} - a_{xy}^{(\mathrm{W})} - a_{xy}^{(\mathrm{NE})} - a_{xy}^{(\mathrm{SE})} \\ & - a_{xy}^{(\mathrm{NW})} - a_{xy}^{(\mathrm{SW})} \\ & - k^2 \left[\frac{w\left(n\epsilon_{yx}^{(1)}\epsilon_{yy}^{(2)} + s\epsilon_{yx}^{(2)}\epsilon_{yy}^{(1)}\right)}{v_{21}(e+w)} \right. \\ & \left. + \frac{e\left(s\epsilon_{yx}^{(3)}\epsilon_{yy}^{(4)} + n\epsilon_{yx}^{(4)}\epsilon_{yy}^{(3)}\right)}{v_{34}(e+w)} \right] \end{aligned} \tag{34}$$

$$v_{21} \equiv n\epsilon_{yy}^{(2)} + s\epsilon_{yy}^{(1)}, \quad v_{34} \equiv n\epsilon_{yy}^{(3)} + s\epsilon_{yy}^{(4)}. \tag{35}$$

The remaining 18 finite difference coefficients describing A_{yx} and A_{yy} can be obtained by applying the following transformations to (21)–(34):

$$\begin{aligned} x &\leftrightarrow y \\ n, \mathrm{N} &\leftrightarrow e, \mathrm{E} \\ s, \mathrm{S} &\leftrightarrow w, \mathrm{W} \\ \epsilon^{(3)} &\leftrightarrow \epsilon^{(1)} \\ v_{21} \equiv n\epsilon_{yy}^{(2)} + s\epsilon_{yy}^{(1)} &\rightarrow h_{23} \equiv e\epsilon_{xx}^{(2)} + w\epsilon_{xx}^{(3)} \\ v_{34} \equiv n\epsilon_{yy}^{(3)} + s\epsilon_{yy}^{(4)} &\rightarrow h_{14} \equiv e\epsilon_{xx}^{(1)} + w\epsilon_{xx}^{(4)}. \end{aligned} \tag{36}$$

For example, applying the above transformation to (28) gives

$$a_{yx}^{(\mathrm{E})} = \frac{\dfrac{w\epsilon_{xx}^{(2)}\epsilon_{xx}^{(4)}}{h_{23}h_{14}} - \dfrac{w\epsilon_{xx}^{(3)}\epsilon_{xx}^{(1)}}{h_{23}h_{14}} + \dfrac{\epsilon_{xx}^{(1)}\epsilon_{xx}^{(4)}}{\epsilon_{zz}^{(4)}h_{14}} - \dfrac{\epsilon_{xx}^{(2)}\epsilon_{xx}^{(3)}}{\epsilon_{zz}^{(3)}h_{23}}}{(n+s)}. \tag{37}$$

In the limit that $\epsilon_{xx} = \epsilon_{yy} = \epsilon_{zz} \equiv \epsilon$ and $\epsilon_{xy} = \epsilon_{yx} = 0$, these finite difference equations reduce to those presented in [16] and [17] for isotropic waveguides.

Complete source code for implementing this method, together with the additional finite difference equations needed to compute the remaining four field components, is available on the authors' website [31].

ACKNOWLEDGMENT

The authors thank Y. Lu and J. C. Montoya for carefully reading and correcting the manuscript.

REFERENCES

[1] R. Scarmozzino, A. Gopinath, R. Pregla, and S. Helfert, "Numerical techniques for modeling guided-wave photonic devices," *J. Sel. Topics Quantum Electron.*, vol. 6, no. 1, pp. 150–162, 2000.

[2] L. Thylen and D. Yevick, "Beam propagation method in anisotropic media," *Appl. Opt.*, vol. 21, no. 15, pp. 2751–2754, 1982.

[3] C. L. Xu, W. P. Huang, J. Chrostowski, and S. K. Chaudhuri, "A full-vectorial beam propagation method for anisotropic waveguides," *J. Lightw. Technol.*, vol. 12, no. 11, pp. 1926–1931, 1994.

[4] Y. Tsuji, M. Koshiba, and N. Takimoto, "Finite element beam propagation method for anisotropic optical waveguides," *J. Lightw. Technol.*, vol. 17, no. 4, pp. 723–728, 1999.

[5] M. Koshiba, K. Hayata, and M. Suzuki, "Approximate scalar finite-element analysis of anisotropic optical waveguides with off-diagonal elements in a permittivity tensor," *IEEE Trans. Microw. Theory Tech.*, vol. MTT-32, no. 6, pp. 587–593, 1984.

[6] K. Hayata, M. Koshiba, M. Eguchi, and M. Suzuki, "Vectorial finite-element method without any spurious solutions for dielectric waveguiding problems using transverse magnetic-field component," *IEEE Trans. Microw. Theory Tech.*, vol. MTT-34, no. 11, pp. 1120–1124, 1986.

[7] T. Angkaew, M. Matsuhara, and N. Kumagai, "Finite-element analysis of waveguide modes: A novel approach that eliminates spurious modes," *IEEE Trans. Microw. Theory Tech.*, vol. MTT-35, no. 2, pp. 117–123, 1987.

[8] W. C. Chew and M. A. Nasir, "A variational analysis of anisotropic, inhomogeneous dielectric waveguides," *IEEE Trans. Microw. Theory Tech.*, vol. 37, no. 4, pp. 661–668, 1989.

[9] F. A. Femandez and Y. Lu, "A variational finite element formulation for dielectric waveguides in terms of transverse magnetic fields," *IEEE Trans. Magn.*, vol. 27, no. 5, pp. 3864–3867, 1991.

[10] Y. Lu and F. A. Fernandez, "An efficient finite element solution of inhomogeneous anisotropic and lossy dielectric waveguides," *IEEE Trans. Microw. Theory Tech.*, vol. 41, no. 6/7, pp. 1215–1223, 1993.

[11] S. Selleri, L. Vincetti, and M. Zoboli, "Full-vector finite-element beam propagation method for anisotropic optical device analysis," *J. Quantum Electron.*, vol. 36, no. 12, pp. 1392–1401, 2000.

[12] V. Schulz, "Adjoint high-order vectorial finite elements for nonsymmetric transversally anisotropic waveguides," *IEEE Trans. Microw. Theory Tech.*, vol. 51, no. 4, pp. 1086–1095, 2003.

[13] J. P. da Silva, H. E. Hernández-Figueroa, and A. M. F. Frasson, "Improved vectorial finite-element BPM analysis for transverse anisotropic media," *J. Lightw. Technol.*, vol. 21, no. 2, pp. 567–576, 2003.

[14] K. Bierwirth, N. Schulz, and F. Arndt, "Finite-difference analysis of rectangular dielectric waveguide structures," *IEEE Trans. Microw. Theory Tech.*, vol. MTT-34, no. 11, pp. 1104–1114, 1986.

[15] A. T. Galick, T. Kerkhoven, and U. Ravaioli, "Iterative solution of the eigenvalue problem for a dielectric waveguide," *IEEE Trans. Microw. Theory Tech.*, vol. 40, no. 4, pp. 699–705, 1992.

[16] P. Lüsse, P. Stuwe, J. Schüle, and H.-G. Unger, "Analysis of vectorial mode fields in optical waveguides by a new finite difference method," *J. Lightw. Technol.*, vol. 12, no. 3, pp. 487–494, 1994.

[17] G. R. Hadley and R. E. Smith, "Full-vector waveguide modeling using an iterative finite-difference method with transparent boundary conditions," *J. Lightw. Technol.*, vol. 13, no. 3, pp. 465–469, 1995.

[18] C. L. da Silva Souza Sobrinho and A. Giarola, "Analysis of biaxially anisotropic dielectric waveguides with Gaussian-Gaussian index of refraction profiles by the finite-difference method," *Proc. Inst. Elect. Eng.*, vol. 140, no. 3, pt. H, pp. 224–230, 1993.

[19] P. Lüsse, K. Ramm, and H.-G. Unger, "Vectorial eigenmode calculation for anisotropic planar optical waveguides," *Electron. Lett.*, vol. 32, no. 1, pp. 38–39, 1996.

[20] M.-C. Oh, S.-S. Lee, and S.-Y. Shi, "Simulation of polarization converter formed by poling-induced polymer waveguides," *J. Quantum Electron.*, vol. 31, no. 9, pp. 1698–1704, 1995.

[21] W. C. Chew, J. M. Jin, and E. Michielssen, "Complex coordinate stretching as a generalized absorbing boundary condition," *Microw. Opt. Technol. Lett.*, vol. 15, no. 6, pp. 363–369, 1997.

[22] M. Loymeyer, N. Bahlmann, O. Zhuromskyy, H. Dötsch, and P. Hertel, "Phase-matched rectangular magnetooptic waveguides for applications in integrated optics isolators: Numerical assessment," *Opt. Comm.*, vol. 158, pp. 189–200, 1998.

[23] R. B. Lehoucq, D. C. Sorensen, and C. Yang, *ARPACK Users' Guide: Solution of Large-Scale Eigenvalue Problems with Implicitly Restarted Arnoldi Methods*. Philadelphia, PA: SIAM, 1998.

[24] T. A. Davis and I. S. Duff, "An unsymmetric-pattern multifrontal method for sparse LU factorization," *SIAM J. Matrix Anal. Appl.*, vol. 18, no. 1, pp. 140–158, 1997.

[25] H. A. Haus and W. Huang, "Coupled-mode theory," *Proc. IEEE*, vol. 79, no. 10, pp. 1505–1518, 1991.

[26] H. Dötsch, N. Bahlmann, O. Zhuromskyy, M. Hammer, L. Wilkens, R. Gerhardt, P. Hertel, and A. F. Popkov, "Applications of magneto-optical waveguides in integrated optics: Review," *J. Opt. Soc. Amer. B*, vol. 22, no. 1, pp. 240–253, 2005.

[27] W.-Y. Hwang, J.-J. Kim, T. Zyung, M.-C. Oh, and S.-Y. Shin, "TE-TM mode converter in a poled-polymer waveguide," *J. Quantum Electron.*, vol. 32, no. 6, pp. 1054–1062, 1996.

[28] H.-H. Oh, S.-W. Ahn, and S.-Y. Shin, "Polarisation-independent phase modulator using electro-optic polymer," *Electron. Lett.*, vol. 36, no. 11, pp. 969–970, 2000.

[29] J. Yang, Q. Zhou, X. Jiang, M. Wang, Y. Wang, and R. T. Chen, "Optical circular-polarization modulator employing tilt-poled electrooptic polymers," *J. Lightw. Technol.*, vol. 22, no. 8, pp. 1930–1934, 2004.

[30] J. W. Wu, "Birefringent and electro-optic effects in poled polymer films: Steady-state and transient properties," *J. Opt. Soc. Amer. B*, vol. 8, no. 1, pp. 142–152, 1991.

[31] [Online]. Available: http://www.photonics.umd.edu/

Arman B. Fallahkhair (S'04) is working toward the Electrical Engineering degree at the University of Maryland, College Park.

He transferred to the University of Maryland after spending a year at the Eastern Mediterranean University, Cyprus. His interests are math, physics, and their applications in theoretical sciences.

Kai S. Li was born in Hong Kong in August 19, 1985. He is working toward the Computer Engineering degree at the New Jersey Institute of Technology, Newark.

His research interests include routing theory, distributed system, programming languages, artificial intelligence, VoIP network and related services, and simulation of optical phenomena.

Thomas E. Murphy (M'94–SM'07) received joint B.A./B.S.E.E. degrees in physics and electrical engineering from Rice University, Houston, TX, in 1994 and the M.S. and Ph.D. degrees in electrical engineering from the Massachusetts Institute of Technology (MIT), Cambridge, in 1997 and 2000, respectively.

In 1994, he joined the NanoStructures Laboratory, MIT, where he pursued research in integrated optics and nanotechnology. In 2000, he joined MIT Lincoln Laboratory as a staff member in the Optical Communications Technology Group where he studied and developed ultrafast optical communications systems. In August 2002, he joined the faculty at the University of Maryland, College Park, as an Assistant Professor in the Department of Electrical and Computer Engineering. His research interests include optical communications, short-pulse phenomena, numerical simulation, optical pulse propagation, nanotechnology and integrated photonics.

Dr. Murphy is a member of the Optical Society of America (OSA), Washington, DC, and a recipient of the NSF CAREER award.